The host dark matter haloes of [O II] emitters at $0.5 < z < 1.5$

V. Gonzalez-Perez,[1,2]★ J. Comparat,[3] P. Norberg,[2,4] C. M. Baugh,[2] S. Contreras,[5] C. Lacey,[2] N. McCullagh,[2] A. Orsi,[6] J. Helly[2] and J. Humphries[2]

[1]*Institute of Cosmology & Gravitation, University of Portsmouth, Dennis Sciama Building, Portsmouth PO1 3FX, UK*
[2]*Institute for Computational Cosmology, Department of Physics, Durham University, South Road, Durham DH1 3LE, UK*
[3]*Max-Planck Institut fur extraterrestrische Physik, Postfach 1312, D-85741 Garching bei Munchen, Germany*
[4]*Centre for Extragalactic Astronomy, Department of Physics, Durham University, South Road, Durham DH1 3LE, UK*
[5]*Instituto de Astrofísica, Pontifica Universidad Católica de Chile, Santiago, Chile*
[6]*Centro de Estudios de Física del Cosmos de Aragón, Plaza de San Juan 1, Teruel E-44001, Spain*

ABSTRACT

Emission line galaxies (ELGs) are used in several ongoing and upcoming surveys (SDSS-IV/eBOSS, DESI) as tracers of the dark matter distribution. Using a new galaxy formation model, we explore the characteristics of [O II] emitters, which dominate optical ELG selections at $z \simeq 1$. Model [O II] emitters at $0.5 < z < 1.5$ are selected to mimic the DEEP2, VVDS, eBOSS and DESI surveys. The luminosity functions of model [O II] emitters are in reasonable agreement with observations. The selected [O II] emitters are hosted by haloes with $M_{\rm halo} \geq 10^{10.3} h^{-1} {\rm M}_\odot$, with ~ 90 per cent of them being central star-forming galaxies. The predicted mean halo occupation distributions of [O II] emitters have a shape typical of that inferred for star-forming galaxies, with the contribution from central galaxies, $\langle N \rangle_{\rm [O II]\,cen}$, being far from the canonical step function. The $\langle N \rangle_{\rm [O II]\,cen}$ can be described as the sum of an asymmetric Gaussian for discs and a step function for spheroids, which plateau below unity. The model [O II] emitters have a clustering bias close to unity, which is below the expectations for eBOSS and DESI ELGs. At $z \sim 1$, a comparison with observed g-band-selected galaxy, which is expected to be dominated by [O II] emitters, indicates that our model produces too few [O II] emitters that are satellite galaxies. This suggests the need to revise our modelling of hot gas stripping in satellite galaxies.

Key words: methods: analytical – methods: numerical – galaxies: evolution – galaxies: formation – cosmology: theory.

1 INTRODUCTION

The quest to understand the nature of both dark matter and dark energy has led us to adopt new tracers of the large-scale structure of the Universe, such as emission line galaxies (hereafter ELGs; e.g. Laureijs et al. 2011; Dawson et al. 2016; DESI Collaboration et al. 2016a; Pozzetti et al. 2016). Current ELG samples are small and their characteristics are not well understood (Comparat et al. 2016b; Kaasinen et al. 2016). Initial tests on relatively small area surveys indicate that there are enough ELGs to chart space–time and understand the transition between the dark matter and the dark energy dominated eras (Comparat et al. 2013; Okada et al. 2016; Delubac

et al. 2017). Moreover, by measuring the properties of ELGs as tracers of star formation over a substantial amount of cosmic time, we can shed light on the mechanisms that quench the star formation in typical galaxies since the peak epoch of star formation around $z \simeq 2$ (Lilly et al. 1996; Madau et al. 1996; Mostek et al. 2013).

The SDSS-IV/eBOSS[1] survey is currently targeting what will become the largest sample to date of ELGs at $z \simeq 0.85$ (Comparat et al. 2016a; Raichoor et al. 2017; Delubac et al. 2017). This large sample will allow us to go beyond the current state-of-the-art cosmological constraints by measuring cosmological probes such as baryon acoustic oscillations and redshift-space distortions at $z \sim 1$ (Zhao et al. 2016). This pioneering use of ELGs as cosmological

★E-mail: violegp@gmail.com

[1] Extended Baryon Oscillation Spectroscopic Survey, http://www.sdss.org/surveys/eboss/ (Dawson et al. 2016).

probes is planned to be enhanced by future surveys, such as DESI,[2] PFS,[3] WEAVE,[4] and 4MOST.[5]

An ELG is the generic name given to any galaxy presenting strong emission lines associated with star-formation events. Galaxies with nuclear activity also present emission lines. However, the line ratios of such objects tend to be different from those driven by star formation activity because of the different ionization states present (e.g. Belfiore et al. 2017). The presence of these features allows for a robust determination of galaxy redshifts. Most of the sampled ELGs at $z \sim 1$ are expected to present a strong [O II] line at a rest-frame wavelength of 3727 Å. For detectors sampling optical to near infrared wavelengths [O II] emitters can be detected up to $z = 2$ (e.g. Sobral et al. 2012).

The fate of galaxies is determined by the growth of dark matter structures which, in turn, is affected by the nature of the dark energy. However, gravity is not the only force shaping the formation and evolution of galaxies. Baryons are affected by a multitude of other processes, mostly related to the fate of gas. Computational modelling is the only way we can attempt to understand all the processes involved in the formation and evolution of galaxies (e.g. Somerville & Davé 2015). The [O II] emission is particularly difficult to predict since it depends critically on local properties, such as dust attenuation and the structure of the H II regions and their ionization fields. This is why [O II] traces star formation and metallicity in a non-trivial way (e.g. Kewley, Geller & Jansen 2004; Dickey et al. 2016).

Previous work on modelling [O II] emitters has shown that semi-analytic galaxy formation models can reproduce their observed luminosity function (LF) at $z \sim 1$ (Orsi et al. 2014; Comparat et al. 2015, 2016b), making them ideal for studying the clustering properties of [O II] emitters and hence bias. These predictions are used in the design and interpretation of current and future surveys, such as eBOSS (Dawson et al. 2016) and DESI (DESI Collaboration et al. 2016a). Favole et al. (2016) inferred the clustering and fraction of saellites for a g-band-selected sample of galaxies that is expected to be dominated by ELGs at $0.6 < z < 1.7$. Their results are based on a modified sub-halo abundance matching (SHAM) technique that takes into account the incompleteness in the selection of ELGs, because not all haloes will contain an ELG. Favole et al. found that their sample of g-band-selected galaxies at $z \sim 0.8$ is best matched by a model with 22.5 ± 2.5 per cent of satellite galaxies and a mean host halo mass of $(1 \pm 0.5) \times 10^{12} h^{-1} M_{\odot}$. With the necessary modifications of the SHAM technique to provide a good description of the clustering of the observed ELGs, which is an incomplete sample of galaxies, the $\langle N \rangle_M$ for central ELGs is expected to differ from the canonical step function which reaches one central galaxy per halo, which is typical in mass-limited samples.

Here, we aim to characterize the nature of model [O II] emitters as tracers of the star formation across cosmic time, and to study their expected mean halo occupation distribution and clustering to better understand [O II] emitters as tracers of the underlying cosmology. We adopt a physical approach rather than the empirical

one used in Favole et al. (2016). The use of a semi-analytical (SA) model of galaxy formation and evolution (see Lacey & Silk 1991; White & Frenk 1991; Kauffmann, White & Guiderdoni 1993; Cole et al. 1994; Somerville & Primack 1999, for some of the early developments in this field) gives us the tools to understand the physical processes that are the most relevant for the evolution of ELGs in general and [O II] emitters in particular. Here we present a new flavour of GALFORM, developed based on Gonzalez-Perez et al. (2014, hereafter GP14), a model that produced [O II] emitter LFs in reasonable agreement with observations (Comparat et al. 2015).

The plan of this paper is as follows.[6] In Section 2 we introduce a new galaxy model (GP17), which is an evolution of previous GALFORM versions. In Section 3.2 the [O II] LFs from different observational surveys are compared to model [O II] emitters selected to mimic these surveys. These selections are explored in both Section 3.3 and Appendix A. Given the reasonable agreement found between this GP17 model and current observations, we infer the mean halo occupation distribution in Section 4.2 and clustering in Section 5 of [O II] emitters. In Section 6 we summarize and discuss our results.

2 THE SEMI-ANALYTIC MODEL

SA models use simple, physically motivated, rules to follow the fate of baryons in a universe in which structure grows hierarchically through gravitational instability (see Baugh 2006; Benson 2010, for an overview of hierarchical galaxy formation models).

GALFORM was introduced by Cole et al. (2000) and since then it has been enhanced and improved (e.g. Baugh et al. 2005; Bower et al. 2006; Fanidakis et al. 2011; Lagos et al. 2011; Lacey et al. 2016). GALFORM follows the physical processes that shape the formation and evolution of galaxies, including: (i) the collapse and merging of dark matter haloes; (ii) the shock-heating and radiative cooling of gas inside dark matter haloes, leading to the formation of galaxy discs; (iii) quiescent star formation in galaxy discs which takes into account both the atomic and molecular components of the gas (Lagos et al. 2011); (iv) feedback from supernovae, from active galactic nuclei (Bower et al. 2006) and from photo-ionization of the intergalactic medium; (v) chemical enrichment of the stars and gas (assuming instantaneous recycling); (vi) galaxy mergers driven by dynamical friction within common dark matter haloes. GALFORM provides a prediction for the number and properties of galaxies that reside within dark matter haloes of different masses.

Currently, there are two main branches of GALFORM: one with a single initial mass function (IMF; GP14) and one that assumes different IMFs for quiescent and bursty episodes of star formation (Lacey et al. 2016).

Here we introduce a new version of the GALFORM model of the formation and evolution of galaxies (This article, hereafter GP17), which will be available in the Millennium Archive Database.[7] The details specific to the GP17 model are introduced in Section 2.1. Below we also give further details of how GALFORM models emission lines (Section 2.2) and dust (Section 2.3) as these are key aspects to understand the results from this study.

Table 1. Differences between the GP17 and the GP14 GALFORM implementation. α_{cool} is one of the parameters setting the AGN feedback efficiency in GALFORM (equation (12) in Lacey et al. 2016) and v_{SN} is related to the modelling of SN feedback (equation (10) in Lacey et al. 2016).

GALFORM parameter	GP14	GP17 (this work)
IMF[a]	Kennicutt	Chabrier
SPS model	BC99[b]	Conroy, Gunn & White
Stripping of hot gas	instantaneous	Gradual
Merging scheme	Lacey & Cole	Simha & Cole
α_{cool} (AGN feedback)	0.6	0.9
v_{SN} (SN feedback) [km/s]	425	370

Notes. [a]The metal yield and recycled fractions are not considered as free parameters here since their values are set by the assumed stellar IMF, following calculations carried out with PEGASE2 (Fioc & Rocca-Volmerange 1999). In GP17 we fix the metal yield to 0.02908 and the recycled fraction to 0.4588. [b]BCC99 is an updated version of the Bruzual A. & Charlot (1993) SPS model.

2.1 The GP17 model

The GP17 model uses dark matter halo merger trees extracted from the MS-W7 *N*-body simulation (Guo et al. 2013; Jiang et al. 2014; GP14), a box of 500 h^{-1}Mpc aside and with a cosmology consistent with the 7th year release from *Wilkinson Microwave Anisotropy Probe* (Komatsu et al. 2011): matter density $\Omega_{m,0} = 0.272$, cosmological constant $\Omega_{\Lambda,0} = 0.728$, baryon density $\Omega_{b,0} = 0.0455$, a normalization of density fluctuations given by $\sigma_{8,0} = 0.810$ and a Hubble constant today of $H(z=0) = 100\,h\mathrm{km\,s^{-1}Mpc^{-1}}$ with $h = 0.704$.

The model in this study, GP17, assumes a single IMF, building upon the GALFORM versions presented in both GP14 and Guo et al. (2016). The two main aspects that are different in the GP17 model with respect to GP14 are: (i) the assumption of a gradual stripping of the hot gas when a galaxy becomes a satellite by merging into a larger halo (Font et al. 2008; Lagos et al. 2014) and (ii) the use of a new merging scheme to follow the orbits of these satellite galaxies (Simha & Cole 2017).

Table 1 summarizes all the differences between the new GP17 model and the GP14 GALFORM implementation. We review below the changes made in the same order as they appear in Table 1.

The GP17 model assumes the IMF from Chabrier (2003). This IMF is widely used in observational derivations, and thus this choice facilitates a more direct comparison between the model results and observational ones. GP17 uses the flexible Conroy et al. (2009) stellar population synthesis (SPS) model (hereafter CW09). Coupling this SPS model to GALFORM gives very similar global properties for galaxies over a wide range of redshifts and wavelengths to using the Bruzual & Charlot (2003) SPS model (as in GP14). The CW09 SPS model was chosen here over that of Bruzual & Charlot (2003) because it provides greater flexibility to explore variations in the stellar evolution assumptions.

2.1.1 The treatment of gas in satellite galaxies

In the GP17 model the hot gas in satellites is removed gradually, using the model introduced by Font et al. (2008) based on a comparison to hydrodynamical simulations of cluster environments (McCarthy et al. 2008). This change has a direct impact on the distribution of specific star formation rates. Compared to the GP14 model, some galaxies from the GP17 model have higher sSFR values, in better agreement with observational inferences (Weinmann et al. 2009). This is clearly seen in the sSFR func-
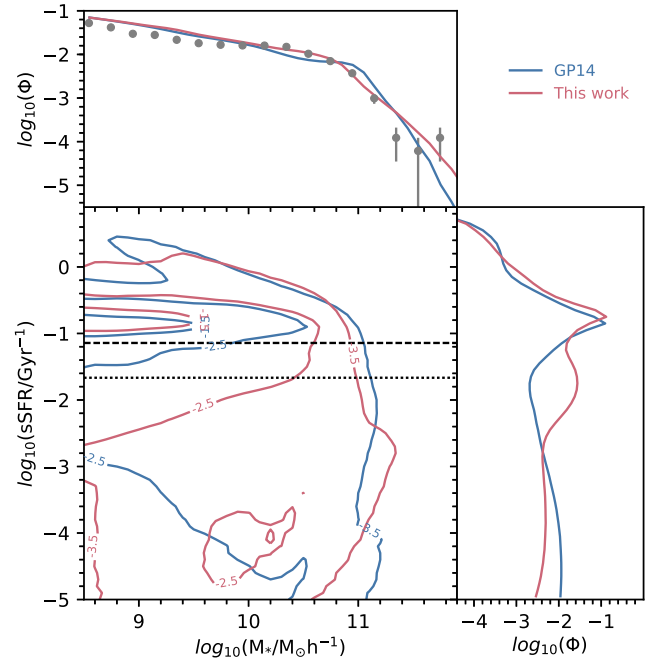

Figure 1. The $z = 0$ distribution of galaxies in the sSFR–stellar mass plane for galaxies from the model presented here (red lines) and that described in GP14 (blue lines). The horizontal dotted line corresponds to the boundary proposed by Franx et al. (2008) to separate star-forming from passively evolving galaxies, sSFR $= 0.3/t_{Hubble}(z)$, while the dashed line simply shows sSFR $= 1/t_{Hubble}(z)$, for comparison. The sSFR–stellar mass plane has been collapsed into the galaxy stellar mass function, top, and the sSFR function, right. The corresponding densities shown are $\Phi(h^3\mathrm{Mpc}^{-3}\mathrm{dex}^{-1})$. The $z = 0$ stellar mass function is compared to results from Baldry et al. (2012), grey symbols. Following Lacey et al. (2016), the estimations from the GP14 model have been corrected from the assumed Kennicutt IMF to the Chabrier one assumed in both observations and the GP17 model.

tion around $\log_{10}(\mathrm{sSFR/Gyr^{-1}}) \sim -1.5$ presented in Fig. 1. This choice reduces the fraction of passive model galaxies with $M_* < 10^{11} h^{-1}\,\mathrm{M_\odot}$. As shown in Fig. 2, the resulting passive fraction is closer to the observational results at $z = 0$, compared with models such GP14, which assumes instantaneous stripping of the hot gas from satellites (see also Lagos et al. 2014; Guo et al. 2016, and discussions therein). Note that we have not made a direct attempt to reproduce the observed passive fraction by adjusting the time-scale for the hot gas stripping in satellite galaxies, but rather we have simply used the parameters introduced in Font et al. (2008). We leave a detailed exploration of the effect of environmental processes on galaxy properties for another study. The passive fraction at $z = 0$ is obtained using the limit on the specific star formation rate, sSFR $= \mathrm{SFR}/M_*$, proposed in Franx et al. (2008), i.e. sSFR $< 0.3/t_{Hubble}(z)$, where $t_{Hubble}(z)$ is the Hubble time, $t_{Hubble} = 1/H$, at redshift z. Fig. 1 shows the $z = 0$ distribution of the sSFR and stellar mass for GP17 model galaxies, together with those from the GP14 model, compared to the limits sSFR $= 0.3/t_{Hubble}(z)$ and sSFR $< 1/t_{Hubble}(z)$ (horizontal dotted and dashed lines, respectively). The contours show that the main sequence of star-forming galaxies, i.e. the most densely populated region in the sSFR–M_* plane, is above both these limits, while passively evolving galaxies, i.e. those with low star formation rates, are below them. Fig. 1 also shows the model galaxy stellar mass function at $z = 0$ compared with observations.
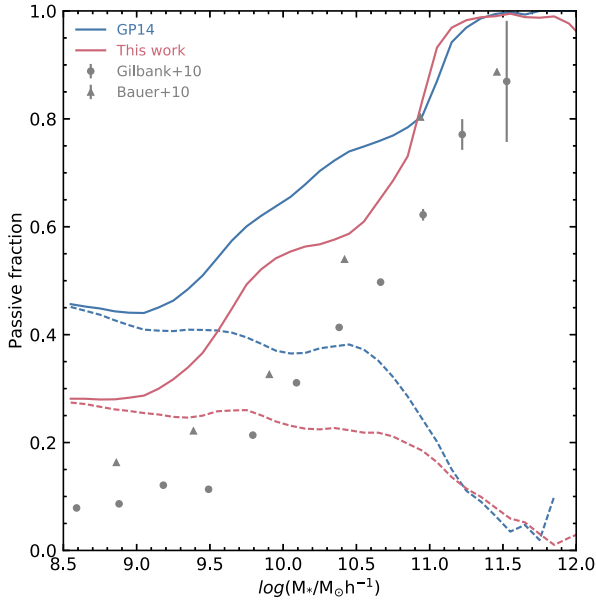
Figure 2. The fraction of passive galaxies at $z = 0$, i.e. those with sSFR $< 0.3/t_{Hubble}(z = 0)$, in the GP17 model (solid red line) and in GP14 (solid blue line), compared to the observational results from Gilbank et al. (2010) and Bauer et al. (2013) (triangles), as extracted and presented in Furlong et al. (2015). The dashed lines show the contribution of satellite galaxies to the total passive fraction.

2.1.2 The merging scheme for satellite galaxies

The GP17 model is the first publicly available GALFORM model to use the new merging scheme introduced by Simha & Cole (2017). In this merging scheme, satellite galaxies associated with resolved sub-haloes cannot merge with the central galaxy until their host sub-halo does. Satellite galaxies with no associated resolved sub-halo merge with their central galaxy after a time calculated analytically, taking into account dynamical friction and tidal stripping. As described in Campbell et al. (2015), compared to observations up to $z = 0.7$, the radial distribution of GALFORM galaxies is too highly concentrated (see also Contreras et al. 2013). As a result of using the merging scheme of Simha & Cole, satellite galaxies merge more quickly with their central galaxy than it was previously assumed by the analytical function used (Lacey & Cole 1993). This, along with the modification to the radial distribution of satellite galaxies, results in an improved match to the observed two-point-correlation function at small scales (Campbell et al. 2015).

2.1.3 Calibration of the free parameters

The free parameters in the GP17 model have been calibrated to reproduce the observed LFs[8] at $z = 0$ in both the b_J and K bands (Norberg et al. 2002; Driver et al. 2012), as shown in Fig. 3, to give reasonable evolution of the UV and V-band LFs and to reproduce the observed black hole–bulge mass relation (not shown here but which matches observations equally well as in GP14). When calibrating the GP17 model, our aim was to make the smallest number of changes to the GP14 model parameters. A side effect of incorporating the merging scheme from Simha & Cole into the model is an

---

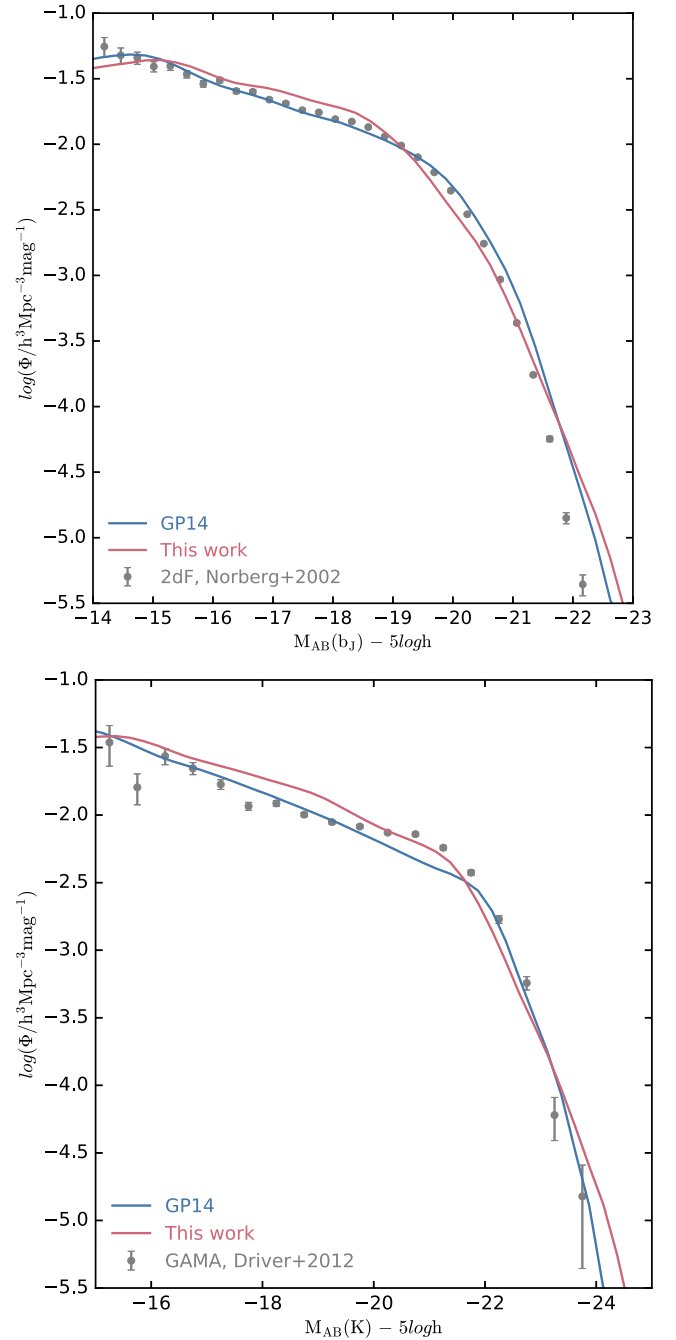8 Note that throughout this work all quoted magnitudes are in the AB system, unless specified otherwise.

Figure 3. The predicted LFs at $z = 0$ (solid lines), in the b_J band ($\lambda_{eff} = 4500$Å, top) and in the K band ($\lambda_{eff} = 2.2$ μm, bottom), compared with observations from Norberg et al. (2002) and Driver et al. (2012), respectively. The blue lines show the predictions from the GP14 model, while the red lines show the predictions from the new GP17 model presented here. These data were used to calibrate the free parameters of the model.

increase in the number of massive central galaxies at $z = 0$, which has to be compensated for by modifying the galactic feedback, in order to recover the same level of agreement with the observational data sets used during the calibration of the model parameters. To achieve this, both the efficiency of the supernova feedback and the mass of haloes within which gas cooling stops due to AGN feedback have been reduced. The changes to these two parameters related to galactic feedback allow for the GP17 model to match the observed

$z = 0$ LFs shown in Fig. 3 with a χ^2 that is just a factor of 3 larger than that for LFs from the GP14 model.

2.2 The emission line model

The GP14 model predicts the evolution of the Hα LF reasonably well (Lagos et al. 2014). Hα is a recombination line and thus its unattenuated luminosity is directly proportional to the number of Lyman continuum photons, which is a direct prediction of the GALFORM model (Orsi et al. 2008, 2010). The main uncertainty in the case of the Hα line is the dust attenuation.

In GALFORM, the ratio between the [O II] luminosity and the number of Lyman continuum photons is calculated using the H II region models of Stasińska (1990). The GALFORM model uses by default eight H II region models spanning a range of metallicities but with the same uniform density of 10 hydrogen particles per cm^{-3} and one ionizing star in the centre of the region with an effective temperature of 45 000 K. The ionizing parameter[9] of these H II region models is around 10^{-3}, with exact values depending on their metallicity in a non-trivial way. These ionizing parameters are typical within the grid of H II regions provided by Stasińska (1990).

In this way, the GALFORM model assumes a nearly invariant ionization parameter. This assumption, although reasonable for recombination lines, is possibly too simplistic in practice for other emission lines such as [O II] (e.g. Sanchez et al. 2015). Nevertheless, with this caveat in mind, we shall study the predictions of GALFORM for [O II] emitters with the simple model here and defer the use of a more sophisticated emission line model to a future paper.

We have also run the galaxy formation model together with the empirical emission line ratios described in Anders & Fritze-v. Alvensleben (2003). These authors provide line ratios for five metallicities, combining the observational data base of Izotov, Thuan & Lipovetsky (1994, 1997) and Izotov & Thuan (1998) for $Z = 0.0004$ and $Z = 0.004$, and using Stasińska (1990) models for higher metallicities, $Z = 0.008, 0.02, 0.05$. Anders & Fritze-v. Alvensleben (2003) provide line ratios with respect to the flux of the Hβ line, which they assume to be 4.757×10^{-13} times the number of hydrogen ionizing photons, N_{Lyc}. For the other hydrogen lines we assume the low-density limit recombination Case B (the typical case for nebulae with observable amounts of gas) and a temperature of 10 000 K: $F(Ly_\alpha)/F(H\beta) = 32.7$, $F(H\alpha)/F(H\beta) = 2.87$, $F(H_\gamma)/F(H\beta) = 0.466$ (tables 4.1 and 4.2 in Osterbrock & Ferland 2006). These line ratios have been reduced by a factor of 0.7 for gas metallicities $Z \geq 0.08$ to account for absorption of ionizing photons within the H II region (Anders & Fritze-v. Alvensleben 2003).

We have done all the analysis presented in this paper using the Anders & Fritze-v. Alvensleben (2003) model for H II regions obtaining very similar results to those presented below when using the default models from Stasińska (1990). Thus, all the conclusions from this work are also adequate when the Anders & Fritze-v. Alvensleben (2003) models are assumed.

2.3 The dust model

Emission lines can only be detected in galaxies that are not heavily obscured and thus survey selections targeting ELGs are likely to

miss dusty galaxies. In GALFORM the dust is assumed to be present in galaxies in two components: diffuse dust (75 per cent) and molecular clouds (25 per cent). This split is consistent, within a factor of 2, with estimates based on observations of nearby galaxies (Granato et al. 2000). The diffuse component is assumed to follow the distribution of stars. Model stars escape from their birth molecular clouds after 1 Myr (the metallicity is assumed to be the same for the stars and their birth molecular clouds). Given the inclination of the galaxy and the cold gas mass and metallicity, the attenuation by dust at a given wavelength is computed using the results of a radiative transfer model (see Gonzalez-Perez et al. 2013, for further details on the modelling of dust attenuation).

Lines are assumed to be attenuated by dust in a similar way to the stellar continuum, as described above. Thus, the predicted [O II] luminosity should be considered as an upper limit as some observational studies find that the nebular emission of star-forming galaxies experiences greater (by up to a factor of 2) dust extinction than the stellar component (Calzetti 1997; De Barros, Reddy & Shivaei 2016). Nevertheless, given the uncertainty in the dust attenuation at the redshifts of interest, the line luminosities are calculated using the model stellar continuum dust attenuation. It is worth noting that, as was also found for cluster galaxies at $z \sim 1$ (Merson et al. 2016), less than 3 per cent of the model ELGs (mostly the brightest [O II] emitters) are attenuated by more than one magnitude in the rest-frame NUV to optical region of the spectra, which is due to the very small sizes and large cold gas content of those galaxies.

3 MODEL [O II] EMITTERS

Star-forming galaxies exhibiting strong spectral emission lines are generically referred to as ELGs. Present and future surveys such as eBOSS, Euclid and DESI target galaxies within a particular redshift range (Laureijs et al. 2011; Dawson et al. 2016; DESI Collaboration et al. 2016a,b). The specific redshift range and the type of detectors used by a survey will determine which spectral lines will be observed. We focus here on those surveys with optical and near-infrared detectors targeting ELGs at $z \sim 1$ which will have prominent [O II] lines. We will refer to these galaxies as [O II] emitters.

Within the redshift range $0.6 \leq z \leq 1.5$, at most 10 per cent of all model galaxies are [O II] emitters, following the definitions of Table 2 (see Section 3.1). This percentage depends on the minimum galaxy mass, which in this case is set by the resolution of the simulation used. Over 99 per cent of model [O II] emitters are actively forming stars (as defined in Section 2) and over 90 per cent are central galaxies.

In Section 3.1 we describe how we select model [O II] emitters. We compare the model LFs at $0.6 \leq z \leq 1.5$ with observations in Section 3.2 and we explore the selection properties in Section 3.3.

3.1 The selection of [O II] emitters

[O II] emitters are selected from the model output to mimic the set of surveys summarized in the first column of Table 2. The DEEP2 survey used the Keck DEIMOS spectrograph to obtain spectra of $\sim 50\,000$ galaxies in four separate fields covering $\sim 2.8\,\text{deg}^2$ (Newman et al. 2013). The VVDS survey was conducted using the VIMOS multi-slit spectrograph on the ESO-VLT, observing galaxies up to $z = 6.7$ over $0.6\,\text{deg}^2$ for the Deep survey and $8.6\,\text{deg}^2$ in the Wide one (VIMOS VLT Deep Survey Database; Le Fèvre et al. 2013). The eBOSS survey is on-going while the DESI survey

---

[9] Following Stasińska (1990), the ionizing parameter at a given radius, r, of the H II region, $U(r)$ is defined here as a dimensionless quantity equal to the ionizing photon flux, Q, per unit area per atomic hydrogen density, n_H, normalized by the speed of light, c: $U(r) = Q/(4\pi r^2 n_H c)$.

Table 2. The cuts applied to the model galaxies in order to mimic the selection of [O II] emitters in the corresponding observational survey, following the results from Comparat et al. (2015). For [O II] emitters, DEEP2 covers the redshift range of $0.7 < z < 1.3$ and VVDS spans $0.5 < z < 1.3$ (Comparat et al. 2015). Low-redshift galaxies are avoided in the DEEP2 survey by imposing a colour–colour cut. However, here we simply make a cut in the studied redshift. For the case of the eBOSS and DESI selections, very blue [O II] emitters at the target redshift range are discarded due to stellar contamination (further details can be found in Appendix A). Thus, we apply here the colour cuts described in Comparat et al. (2016a) for the eBOSS selection and those described in DESI Collaboration et al. 2016a) for the DESI selection. The magnitudes are on the AB system. The particular filter response used for the different cuts is indicated by a superscript on the magnitude column.

Cuts to mimic	Apparent magnitude	[O II] flux (erg s^{-1}cm^{-2})	Colour selection
DEEP2	$R_{AB}^{DEIMOS} < 24.1$	2.7×10^{-17}	None
VVDS-Deep	$i_{AB}^{CFHT} \leq 24$	1.9×10^{-17}	None
VVDS-Wide	$i_{AB}^{CFHT} \leq 22.5$	3.5×10^{-17}	None
eBOSS	$22.1 < g_{AB}^{DECam} < 22.8$	1×10^{-16}	$0.3 < (g - r) < 0.7$ & $0.25 < (r - z) < 1.4$ & $0.5(g - r) + 0.4 < (r - z) < 0.5(g - r) + 0.8$
DESI	$r_{AB}^{DECam} < 23.4$	8×10^{-17}	$(r - z) > 0.3$ & $(g - r) > -0.3$ & $0.9(g - r) + 0.12 < (r - z) < 1.345 - 0.85(g - r)$

has not yet started. Appendix A details the eBOSS and DESI selections, summarized in Table 2. Model [O II] emitters are selected using the same observational magnitude cuts (second column in Table 2), omitting colour cuts designed to remove low-redshift galaxies as in this study galaxies are selected from the relevant redshift range already. For eBOSS and DESI selections we include the colour cuts designed to remove stellar contaminants (fourth column in Table 2; see Appendix A for further details). A limit on [O II] flux has been added (third column in Table 2) to select model galaxies with a completeness that mimics the constraints from observational surveys.

In the redshift range considered, over 85 per cent of all model galaxies are found to be star-forming. From these, a very small percentage, less than 1 per cent in most cases, is classified as [O II] emitters by the restrictive VVDS-Wide, eBOSS and DESI selections. Given the mass resolution of our model, for the VVDS-Deep and DEEP2 cuts, [O II] emitters account for at most 11 per cent of the total star-forming population at $z = 0.62$, and this percentage decreases with increasing redshift.

3.2 Luminosity functions

The LF for [O II] emitters at $z = 0.62$ from the GP17 model is compared in Fig. 4 to the observational compilation done by Comparat et al. (2016b),[10] which includes data from the VVDS-Deep, VVDS-Wide and DEEP2 surveys among others (Ly et al. 2007; Gilbank et al. 2010; Sobral et al. 2012; Ciardullo et al. 2013; Drake et al. 2013; Khostovan et al. 2015). The model LFs are in reasonable agreement with the observations, with differences within a factor of 5 for densities above 10^{-5}Mpc$^{-3}h^3$dex^{-1}. Given the similarities between the GP17 and GP14 models, this was expected, as the GP14 model was already shown to be in reasonable agreement with observations at $z \sim 1$ (Comparat et al. 2015).

Galaxies with an ongoing starburst dominate the bright end of the model [O II] LF, $L[O II] > 10^{42}h^{-2}$erg s^{-1}, producing the change in the slope of the LF seen at low number densities in Fig. 4. The bright end of the LFs of [O II] emitters selected with the DEEP2, VVDS-Wide and VVDS-Deep cuts is also dominated (at the ∼80 per cent level) by spheroid galaxies (i.e. those with a bulge
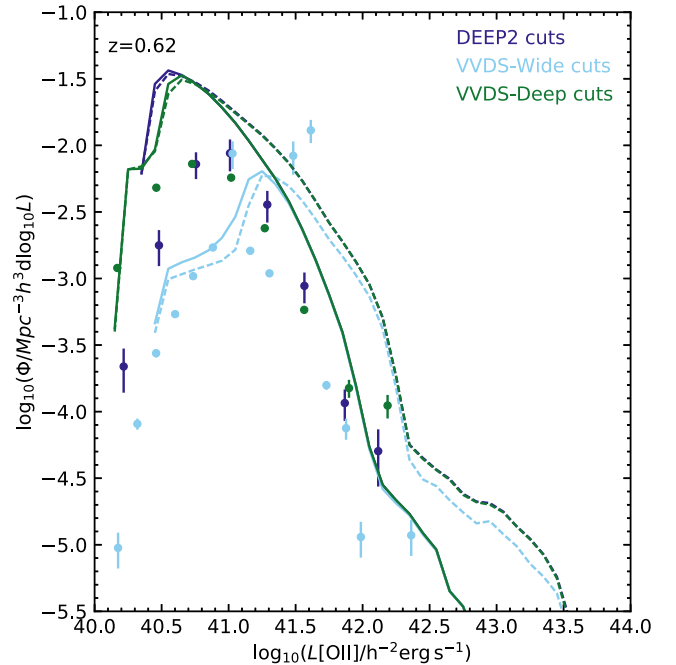

Figure 4. The LF of [O II] emitters at $z = 0.62$ for model galaxies selected with the DEEP2 (dark blue, mostly over-plotted), VVDS-Wide (light blue) and VVDS-Deep (green) cuts given in Table 2. The solid lines present the model [O II] dust attenuated LF, while the dashed lines show the intrinsic LF without considering dust attenuation. Observational data from Comparat et al. (2016b) are shown as filled circles, with colours matching the cuts used to mimic the corresponding survey selection, as indicated in the legend. The observational errors come from jackknife re-sampling (Comparat et al. 2016b) and in some cases are smaller than the symbol.

to total mass above 0.5). More than half of these [O II] emitters with $L[O II] > 10^{42}h^{-2}$erg s^{-1} have half-mass radii smaller than $3h^{-1}$kpc.

The DEEP2 cut uses the DEIMOS R-band filter response, while the VVDS cuts use the CFHT MegaCam[11] i-band filter response. The value of the luminosity at which there is a turnover in the number of faint galaxies is sensitive to the particular filter response

---

[10] http://projects.ift.uam-csic.es/skies-universes/SUwebsite/index.html

[11] http://svo2.cab.inta-csic.es/svo/theory/fps3/index. php?mode=browse&gname=CFHT&gname2=MegaCam

used. Above this luminosity, the model LF changes by less than 0.1 dex in number density if the R or i bands from DEIMOS, CFHT, PAN-STARRS or DES camera are used (note that not all these bands are used for Fig. 4).

We note that BC99, an updated version of the Bruzual A. & Charlot (1993) SPS model, is used by default in most GALFORM models. As the spectral energy distribution below 912 Å can widely vary among different SPS models (GP14), we verified that using the CW09 SPS model (as done in GP17) has a negligible impact on the LF of [O II] emitters. Finally, Fig. 4 shows that at $z = 0.62$ the model reproduces reasonably well the observed LF for [O II] emitters, including the decline in numbers due to the corresponding flux limits (summarized in Table 2).

In Fig. 5 the predicted LFs of [O II] emitters are shown at $z = 0.76$, 0.91, 1.17 and 1.5, sampling the relevant redshift ranges of the current eBOSS and future DESI surveys. The emitter LFs include effects from the five selection criteria summarized in Table 2 and are compared to the observational data compiled by Comparat et al. (2016b). Fig. 5 shows only the LFs with dust attenuation included. As noted before, since the model assumes the same attenuation for the emission lines as for the stellar continuum, the predicted [O II] LFs in Fig. 5 should be considered as overestimates (Calzetti 1997; De Barros et al. 2016). Nevertheless, the predicted continuum extinction is significant and arguably larger than suggested by observations at $z \sim 1$, which might compensate for the lack of any additional attenuation being applied to the emission line luminosities in the model.

3.3 Exploring the ELG selection

The [O II] emitters selected with the cuts presented in Table 2 are star-forming galaxies (e.g. Kewley et al. 2004; Moustakas et al. 2006; Mostek et al. 2012). Fig. 6 shows this by presenting the GP17 model SFR-stellar mass plane for all galaxies at $z = 0.76$ and [O II] emitters selected by four of the cuts summarized in Table 2. Similar trends are found over the redshift range $0.6 \leq z \leq 1.5$, whenever a sufficiently high galaxy number density is used. Most selections are dominated by the cut in line flux. For the mass resolution of our model, in the case of the VVDS-Deep and DEEP2 cuts, the fraction of star-forming galaxies classified as [O II] emitters varies by less than 2 per cent when only the cut in flux is applied. The eBOSS and the DESI selections remove the brightest, $L[\text{O II}] > 10^{42} h^{-2} \text{erg s}^{-1}$, and the most strongly star-forming galaxies with their [O II] emitters selection criteria, as seen in Figs 5 and 6.

The effect of simply imposing a cut in flux in the SFR–stellar mass plane can be seen in Fig. 7. We find a clear correlation between the [O II] luminosity and the average SFR such that a cut in [O II] luminosity is approximately equivalent to selecting galaxies with a minimum SFR. This is with the exception of the most massive galaxies, which are removed when imposing a cut in [O II] luminosity (as shown in the top panel of Figs 4 and 7). Indeed, the most massive galaxies in the model are also those most affected by dust attenuation, in agreement with observational expectations (Sobral et al. 2016).

The ELG samples summarized in Table 2 are limited by their optical apparent magnitudes. Figs 6 and 7 show how this cut in apparent magnitude further reduces the number of low-mass galaxies, with respect to a cut only in the [O II] luminosity. Brighter galaxies in the optical tend to be brighter [O II] emitters and thus galaxies with either low masses or low SFR tend to be removed with a cut in apparent optical magnitude.
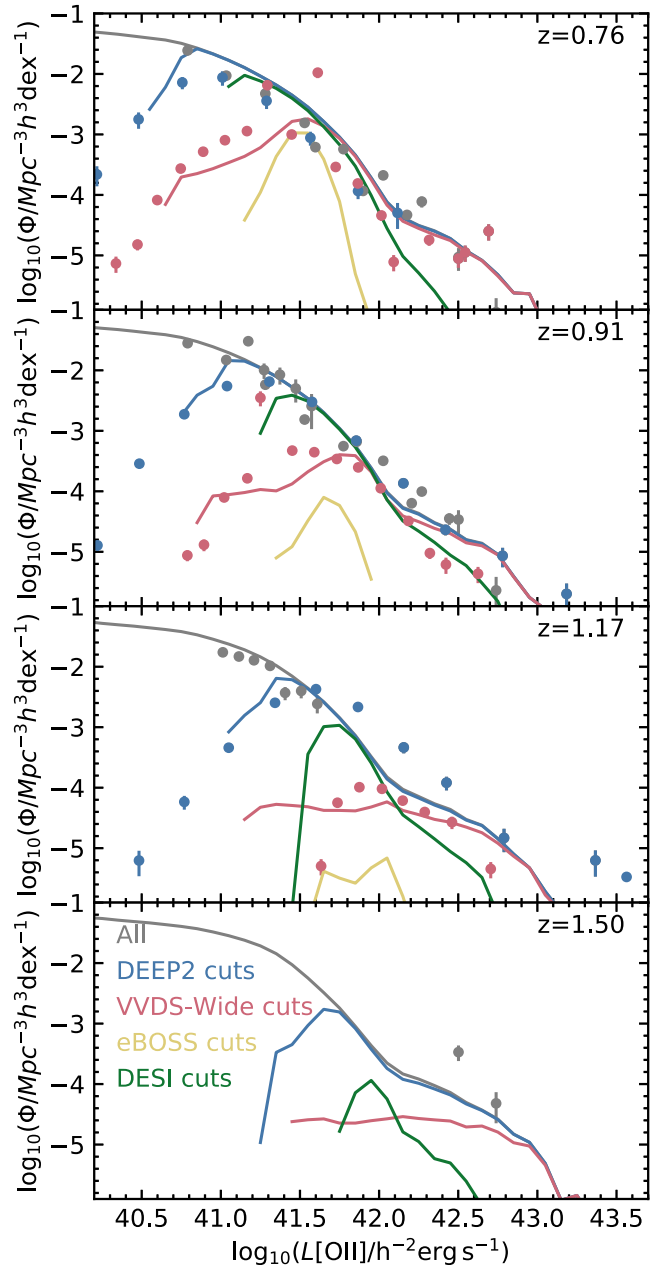

Figure 5. From top to bottom: the LF of [O II] emitters at $z = 0.76$, 0.91, 1.17 and 1.50, for all model galaxies (grey lines), and those selected imposing the Table 2 cuts mimicking DEEP2 (blue), VVDS-Wide (red), eBOSS (yellow) and DESI (green). The grey circles show the observed [O II] emitters LF constructed using complete data in particular luminosity bins by Comparat et al. (2016b). Data from DEEP2 and VVDS are colour coded like the model galaxies selected to mimic both surveys. The observational errors come from jackknife re-sampling (Comparat et al. 2016b) and in some cases are smaller than the symbol.

The distribution of model optical colours remains rather flat with [O II] luminosity, and imposing the eBOSS colour cuts at a given redshift reduces the number of selected galaxies in a non-trivial way within the sSFR–stellar mass parameter space. We remind the reader that some of these colour cuts are actually imposed to remove not only low-redshift galaxies, including ELGs, but also to avoid stellar contamination, as described in Appendix A.
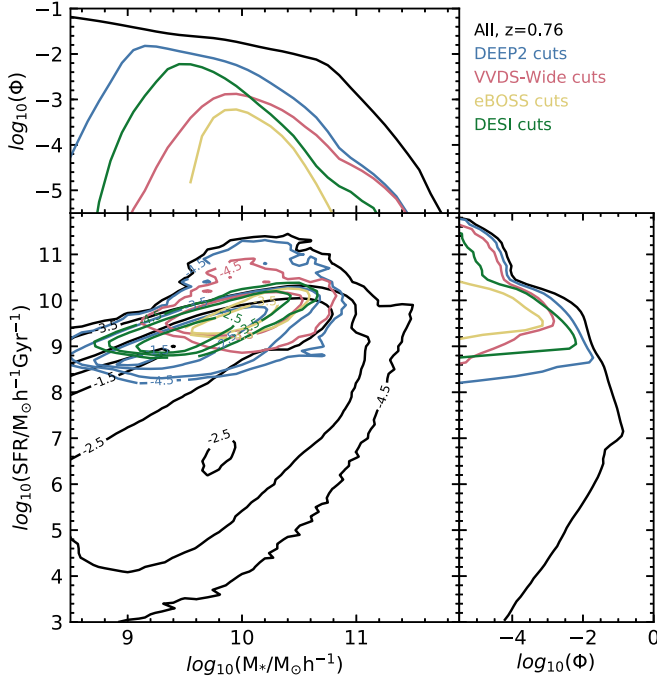
Figure 6. The galaxy distribution in the star-formation rate (SFR)–stellar mass ($M_\star$) plane at $z = 0.76$: the density contours, shown as $\log_{10}(\Psi/h^3\mathrm{Mpc}^{-3}\mathrm{dex}^{-2})$, are for all galaxies (black) and for survey-specific selections, each colour coded following the key. The SFR–$M_\star$ plane has been collapsed into the galaxy stellar mass function, top panel, and the SFR function, right panel, with Φ in units of $h^3\mathrm{Mpc}^{-3}\mathrm{dex}^{-1}$. Basically, all survey selections result primarily in the inclusion of only star-forming model galaxies, but with different levels of sample completeness.
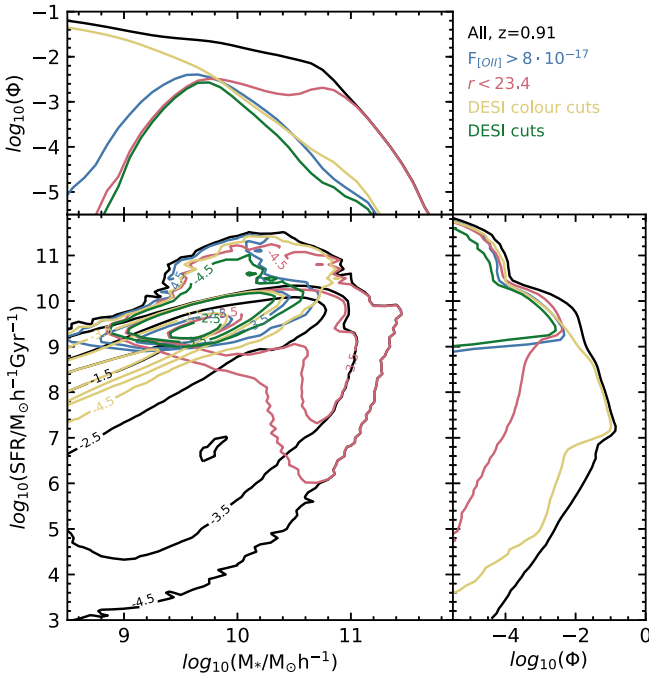
Figure 7. Similar to Fig. 6 but illustrating the separated effects of the different DESI cuts. All model galaxies at $z = 0.91$ are shown in black. Lines of the colours indicated in the legend show galaxies selected with $F_{[O II]} > 8 \times 10^{17}\mathrm{erg\,s}^{-1}\mathrm{cm}^{-2}$, $r < 23.4$, only the DESI colour cuts and the full DESI cuts as summarized in Table 1.

Table 3. The logarithm in base 10 of the mean mass (in units of $\mathrm{M}_\odot h^{-1}$) of the haloes hosting the model [O II] emitters for the selections presented in Table 2. Values are shown at $z = 0.76, 0.91, 1.17$ and 1.50 for those selected [O II] emitters with a global density above $10^{-4}\mathrm{Mpc}^{-3}h^3$.

Selection	$z = 0.76$	$z = 0.91$	$z = 1.17$	$z = 1.50$
DEEP2	11.41	11.49	11.55	11.61
VVDS-Deep	11.49	11.54	11.58	11.64
VVDS-Wide	11.71	11.78	–	–
eBOSS	11.65	11.74	–	–
DESI	11.46	11.56	11.63	–

Further ELG selection characteristics include: (i) the DEEP2 and VVDS-Deep cuts select over 95 per cent of [O II] emitters that form stars quiescently; (ii) galaxies with discs with radii greater than $3h^{-1}\mathrm{kpc}$ account for ~ 60 per cent of the [O II] emitters; (iii) the VVDS-Wide cut selects the brightest model [O II] emitters at the highest redshifts, while the eBOSS and DESI cuts remove the brightest model [O II] emitters with $L[\mathrm{OII}] > 10^{42}h^{-2}\mathrm{erg\,s}^{-1}$. We note also that the brightest [O II] emitters are dominated by spheroids that experience a burst of star formation.

Given the above, a rough approximation to select [O II] emitters samples at $z \sim 1$ is to impose a cut in stellar mass, typically $M_S < 10^{11}h^{-1}\mathrm{M}_\odot$ (since massive galaxies in the model tend to be too attenuated and thus too faint to be selected as [O II] emitters) and SFR (which is tightly correlated to the cut in [O II] luminosity), at least $\mathrm{SFR} > 1h^{-1}\mathrm{M}_\odot\mathrm{yr}^{-1}$.

4 THE HOST HALOES OF [O II] EMITTERS

Model [O II] emitters at $0.5 < z < 1.5$ are hosted by haloes with masses above $10^{10.3}h^{-1}\mathrm{M}_\odot$ and mean masses in the range $10^{11.41} \leq M_{\mathrm{halo}}(h^{-1}\mathrm{M}_\odot) \leq 10^{11.78}$, as summarized in Table 3. From this table it is clear that the host halo mean masses slightly increase with redshift in the studied range. These model masses are consistent with the estimation from Khostovan et al. (2017) for [O II] emitters at $z = 1.47$.

In this section, the masses of haloes hosting [O II] emitters selected as indicated in Table 2 are further explored through the stellar mass–halo mass relation and mean halo occupation distribution.

4.1 The stellar mass–halo mass relation

The stellar-to-halo mass relation for model [O II] emitters is presented in Fig. 8 at $z = 0.76$, together with the global relation for central galaxies. We only show central galaxies in this plot as the sub-haloes hosting satellite galaxies are being disrupted due to tidal stripping and dynamical friction.

At low halo masses, the stellar-to-halo mass relation for the model [O II] emitters flattens out as the cut in the emission line flux effectively imposes a lower limit on the stellar mass of the selected galaxies (see Fig. 7). Above this flattening the stellar mass of model galaxies increases with their host halo mass, with a change of slope around $M_{\mathrm{halo}} \sim 10^{12}h^{-1}\mathrm{M}_\odot$, where star formation is most efficient at this redshift (e.g. Behroozi et al. 2010; Moster et al. 2013; Rodríguez-Puebla et al. 2017). At this halo mass the dispersion in the stellar-to-halo mass relation increases, being about 1.1 dex for all centrals in the model and between 0.5 and 0.8 dex for central [O II] emitters. This is a behaviour particular to GALFORM and it is related to the modelling of the growth of bulges (see Guo et al. 2016; Mitchell et al. 2016, for a more detailed discussion).
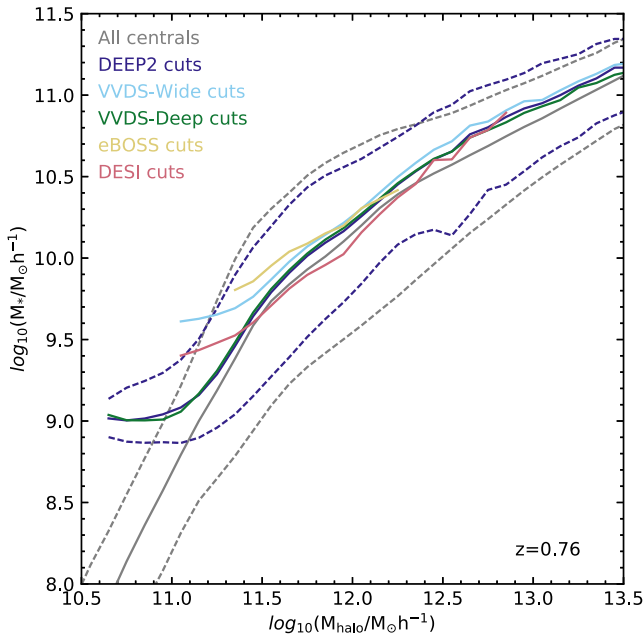
Figure 8. The median stellar-to-halo mass relation for central galaxies in the GP17 model at $z = 0.76$ (grey solid lines), with the 10th and 90th percentiles (grey dashed lines). The median relations for model central galaxies selected with specific survey cuts (see Table 2) are shown by the solid lines, colour coded following the key. For clarity, the 10th and 90th percentiles are shown only for the DEEP2 selection cut, and only halo mass bins with at least 100 galaxies are plotted.

For haloes with $M_{halo} \sim 10^{12.5} h^{-1} M_{\odot}$, the median stellar mass of model [O II] emitters is ~ 1.5 greater than that of the global population. This is driven by the cut in [O II] flux removing low-mass galaxies. The selection of [O II] emitters removes the most massive star-forming galaxies because they are dusty on average and thus, the difference with respect to the global population is smeared out.

4.2 The mean halo occupation distribution

The mean halo occupation distribution, $\langle N \rangle_M$, encapsulates the average number of a given type of galaxy hosted by haloes within a certain mass range. $\langle N \rangle_M$ is usually parametrized separately for central, $\langle N \rangle_{cen}$, and satellite galaxies, $\langle N \rangle_{sat}$. When galaxies are selected by their luminosity or stellar mass, $\langle N \rangle_{cen}$ can be approximately described as a smooth step function that reaches unity for massive enough host haloes, while $\langle N \rangle_{sat}$ is close to a power law (e.g. Berlind et al. 2003; Zheng et al. 2005). However, when galaxies are selected by their star formation rates, $\langle N \rangle_{cen}$ does not necessarily reach unity (e.g. Zheng et al. 2005; Contreras et al. 2015; Cowley et al. 2016). This implies that haloes above a certain mass will not necessarily harbour a star-forming galaxy or, in our case, an ELG. For star-forming galaxies, the shape of the $\langle N \rangle_{cen}$ as a function of halo mass can also be very different from a step function and in some cases it can be closer to a Gaussian (e.g. Geach et al. 2012; Contreras et al. 2013).

Fig. 9 shows the $\langle N \rangle_M$ for model [O II] emitters, $\langle N \rangle_{[O II]}$, selected following the specific survey cuts detailed in Table 2. $\langle N \rangle_{[O II]}$ does not reach unity for all the survey selections in the explored redshift range (see also Fig. 10). This result is fundamental for interpreting the observed clustering of ELGs, as the standard expectation for $\langle N \rangle_{cen}$ is to tend to unity for large halo masses. This point is further
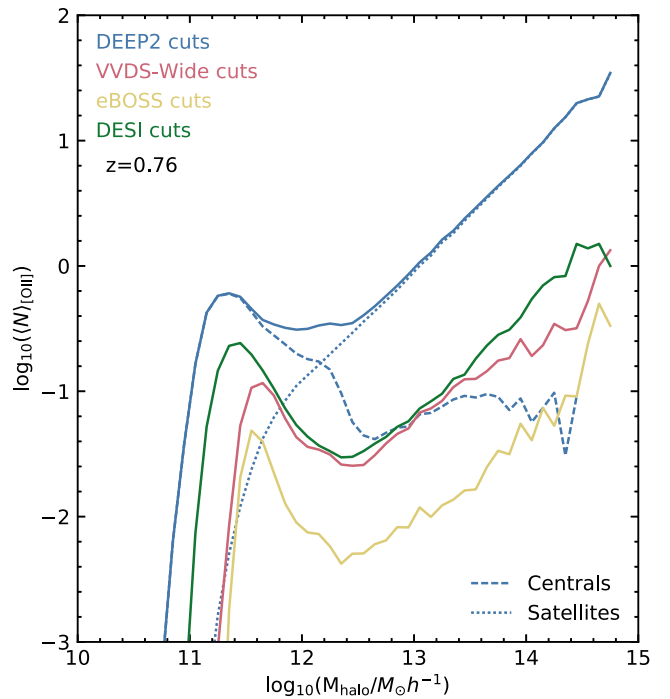

Figure 9. The mean halo occupation distribution, $\langle N \rangle_M$ (solid lines), for galaxies at $z = 0.76$ selected using the cuts indicated in the legend (see Table 2 for their definitions). For galaxies selected using the DEEP2 cuts, the contributions from central and satellite galaxies are shown as dashed and dotted lines, respectively.
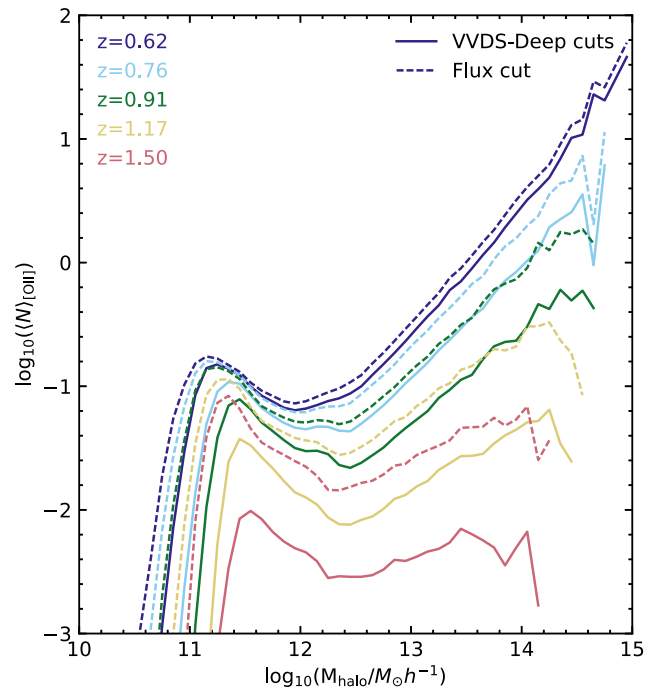

Figure 10. The redshift evolution (colour coded according to the legend, covering the range $z = 0.62$ to $z = 1.5$ from top to bottom) of the mean halo occupation distribution of [O II] emitters ($\langle N \rangle_{[O II]}$) selected with the VVDS-Deep cuts (solid lines) and with only a flux cut of $F_{[O II]} > 1.9 \times 10^{-17} \, \mathrm{erg \, s^{-1} \, cm^{-2}}$ (dashed lines).

emphasized by splitting $\langle N \rangle_{[O\,II]}$ for galaxies selected with DEEP2-like cuts into satellites and centrals. The $\langle N \rangle_M$ of model central [O II] emitters, $\langle N \rangle_{[O\,II]\,cen}$, is very different from the canonical smooth step function, which is usually adequate to describe stellar mass threshold samples and is the basis of (sub) halo abundance matching (e.g. Vale & Ostriker 2004; Conroy et al. 2006). We further discuss $\langle N \rangle_{[O\,II]\,cen}$ in Section 4.3.

On the other hand, the predicted $\langle N \rangle_{sat}$ of [O II] emitters closely follows the canonical power law above a minimum halo mass that is typically an order of magnitude larger than the minimum halo mass required to host a central galaxy with the same selection. In the cases studied, less than 10 per cent of the modelled [O II] emitters are satellite galaxies, and thus there are very few haloes hosting even one satellite [O II] emitter.

The redshift evolution of the $\langle N \rangle_{[O\,II]}$ is presented in Fig. 10 for both galaxies selected with the VVDS-Deep cuts and for a simple cut in the [O II] flux line, $F_{[OII]} > 1.9 \times 10^{-17} \mathrm{erg\,s^{-1}cm^{-2}}$. There is a clear drop with redshift for all halo masses in the average halo occupancy of model [O II] emitters. This is mostly driven by the survey magnitude cut, as a simple flux cut reduces the mean occupation much more gradually with redshift. Over the redshift range probed, the minimum mass of haloes hosting [O II] emitters increases with redshift, as they are selected for a fixed cut in either [O II] flux line alone or also in apparent magnitude.

Finally, we note that similar $\langle N \rangle_{[O\,II]}$ shapes are seen for the other cuts considered in this redshift range, with the main change being in the average number of galaxies occupying a given mass halo.

4.3 [O II] central galaxies

As seen in Fig. 9 already, the $\langle N \rangle_{[O\,II]\,cen}$ is clearly different from a step function. Note that this shape cannot be recovered if a cut in SFR and stellar mass is applied, similar to the rough approximation to select [O II] emitters suggested at the end of Section 3.3. The shape of $\langle N \rangle_{[O\,II]\,cen}$ seen in Fig. 9 for model central [O II] emitters is closer to a Gaussian plus a step function or even a power law. This might point to the contribution of at least two different types of model central [O II] emitters. We have explored splitting central [O II] emitters in different ways, including separating those experiencing a burst of star formation. When splitting central [O II] emitters into discs and spheroid galaxies, using a bulge over total mass ratio of 0.5 to set the disc–spheroid boundary, we recover an $\langle N \rangle_{[O\,II]\,cen}$ that can be roughly described as an asymmetric Gaussian, for disc centrals, plus a step function that rises slowly to a plateau, for bulges or spheroid centrals. This is shown in Fig. 11 for [O II] emitters selected with DEEP2 cuts at $z = 0.62$, but similar results are found for other selections and redshifts, as long as the number density of galaxies is sufficiently large for the split to remain meaningful.

Surveys such as eBOSS and DESI will obtain low-resolution spectra for [O II] emitters which are unlikely to be sufficient to gather the information needed to split the population into discs and spheroids. Within the studied redshift range, model [O II] emitters that are central discs tend to be less massive, have lower stellar metallicities and have larger sizes than central spheroids, for all the selections presented in Table 2. In particular, for a given halo mass central galaxies that are spheroids have stellar masses up to a factor of 1.6 larger than central discs. However, since the bulge to total mass ratio varies smoothly with stellar mass, the distributions of these model properties have a large overlap for central discs and spheroids and, thus, it is unclear if they could be used observationally to split the central [O II] emitters population.
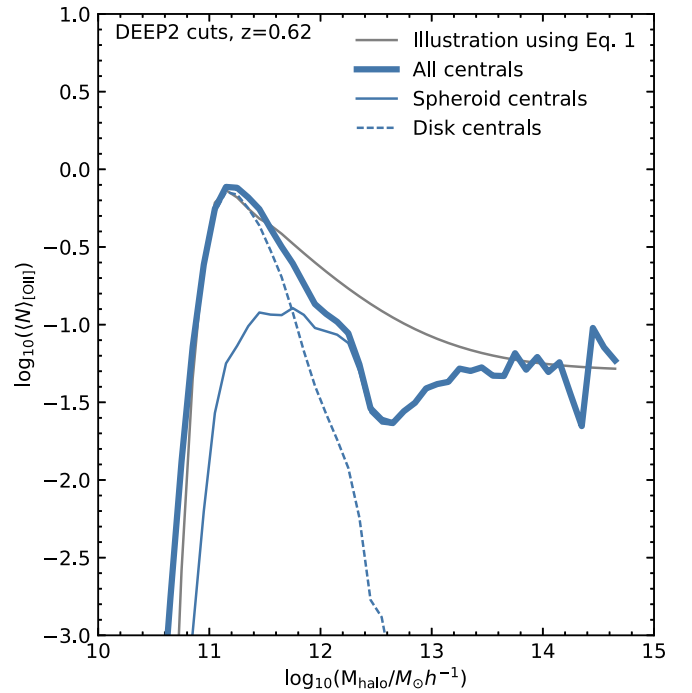

Figure 11. The $\langle N \rangle_M$ for central [O II] emitters selected with the DEEP2 cuts at $z = 0.62$ (thick line). The $\langle N \rangle_{cen}$ is split into the contribution from spheroid-dominated (solid) and disc-dominated (dashed) galaxies. The latter correspond to galaxies with a bulge over total mass less or equal to 0.5. An illustration of equation (1) is shown in grey (see Section 4.3).

A split into three components might describe better the $\langle N \rangle_{[O\,II]\,cen}$ presented in Fig. 11. However, on top of the $\langle N \rangle_M$ becoming noisy for large halo masses it will already be difficult to split observed central [O II] emitters into discs and spheroids to test our model, as in most cases only spectroscopic information is available. Thus, to encapsulate into an illustrative function the shape of the $\langle N \rangle_M$ for model central [O II] emitters, we have opted to propose a function that adds together a softly rising step function for central spheroids (or bulges), b, with an asymmetric Gaussian for central discs, d:

$$\langle N \rangle_{cen} = \frac{f_b}{2} \left(1 + \mathrm{erf} \left(\frac{\log_{10} M_* - \log_{10} M_b}{\sigma} \right) \right)$$
$$+ \frac{f_d}{2} e^{\frac{\alpha_d}{2} (2\log_{10} M_d + \alpha_d \sigma^2 - 2\log_{10} M_*)}$$
$$\times \mathrm{erfc} \left(\log_{10} M_d + \alpha_d \sigma^2 - \frac{\log_{10} M_*}{\sigma \sqrt{2}} \right). \quad (1)$$

In the above equation, erf is the error function ($\mathrm{erfc} = 1 - \mathrm{erf}$),[12] which behaves like a softly rising step function. M_b gives the characteristic halo mass of the error function for the central bulges, and M_d gives the average halo mass of the Gaussian component for central discs. f_b and f_d control the normalization of the error function and the Gaussian component, respectively. σ controls the rise of the error function and the width of the asymmetric Gaussian. The level of asymmetry of the Gaussian component is controlled by both σ and α_d.

As an illustration, Fig. 11 shows in grey the function described in equation (1) with parameters: $\log_{10} M_b = 11.5$, $\log_{10} M_d = 11.0$,

---

[12] $\mathrm{erf}(x) = \frac{2}{\sqrt{\pi}} \int_0^x e^{-t^2} \mathrm{d}t.$
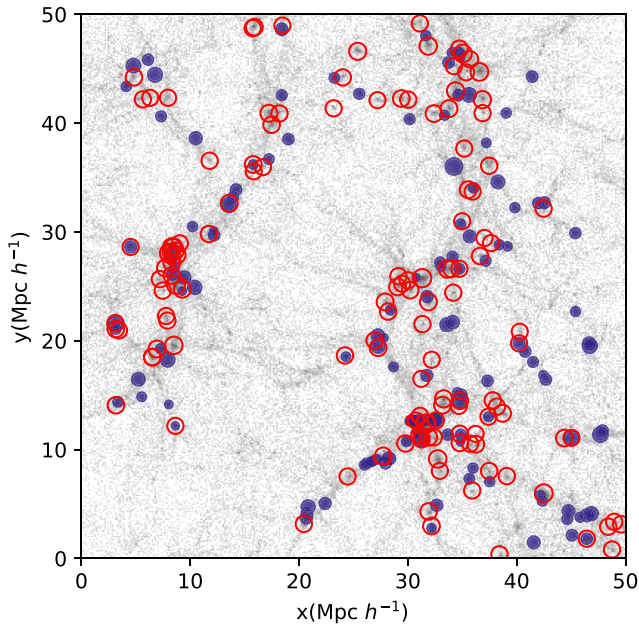
Figure 12. Distribution of [O II] emitters selected with the DEEP2 cuts (filled blue circles) and that of dark matter haloes above $10^{11.8} h^{-1}$ M$_\odot$ (open red circles) painted on top of the smooth underlying dark matter distribution (grey). This slice of $10\, h^{-1}$ Mpc thickness is taken from the MS-W7 simulation at $z = 1$. The halo mass cut is defined so as to match the number density of model [O II] emitters galaxies, i.e. $0.005 h^3$Mpc^{-3}. The circle's area is proportional to $\log_{10}(L_{[OII]})$ and $\log_{10}(M_h)$ for [O II] emitters and dark matter haloes, respectively.

$f_b = 0.05, f_d = 1, \sigma = 0.09, \alpha_d = 1.7$. Adequately fitting the shape of the $\langle N \rangle_{[OII]\,cen}$ with equation (1) is out of the scope of this paper. Moreover, an individual fit to disc and spheroid central galaxies will be more adequate. We defer such an exploration because, as it will be discussed in Section 5, it is unclear that our model is producing a large enough number of [O II] emitters that are also satellite galaxies compared to the expectations from observations. Moreover, the proposed split might not actually be achieved observationally. Nevertheless, given that uncommon features in the mean HOD can affect the inferred galaxy clustering (McCullagh et al. 2017), our proposed equation (1) is a useful tool to explore the impact that such a mean HOD has when interpreting mock catalogues generated for cosmological purposes.

5 THE CLUSTERING OF [O II] EMITTERS

In this section we explore how [O II] emitters trace the dark matter distribution. In Fig. 12 we present a $50 \times 50 \times 10\, h^{-3}$ Mpc^3 slice of the whole simulation box at redshift $z = 1$, highlighting in grey the cosmic web of the dark matter, together with the location of [O II] emitters (filled circles) and of dark matter haloes above $10^{11.8} h^{-1}$ M$_\odot$ (open circles). The environment where model [O II] emitters are found is not the densest as expected for other cosmological tracers such as luminous red galaxies, but instead the [O II] emitters are also found in filamentary structures.

Below we explore the two-point-correlation function monopole in both real and redshift space for model [O II] emitters. The two-point-correlation function has been obtained using two algorithms that give similar results; the plots show the calculation from the publicly available CUTE code (Alonso 2012). The linear bias is also calculated in real space and we compare it with the expectations
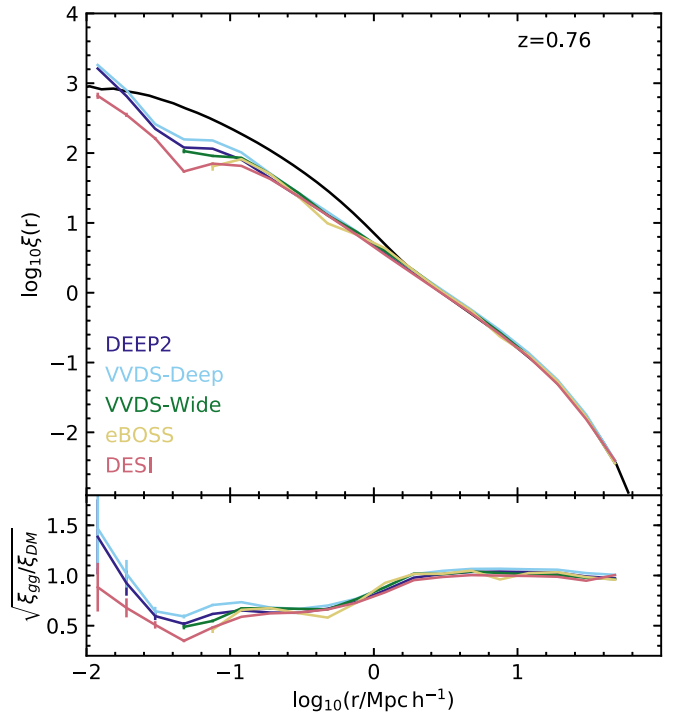

Figure 13. Top panel: the real-space two-point-correlation function at $z = 0.76$ for model galaxies from each of the selections indicated in the legend (see Table 2) together with that of the underlying dark matter (black line). Bottom panel: the real-space bias, $\sqrt{\xi_{gg}/\xi_{DM}}$, at the same redshift. Poisson errors are shown in both panels.

for eBOSS and DESI (Section 5.1). Favole et al. (2016) measured the redshift-space monopole for a sample at $z \sim 0.8$ of g-band-selected galaxies that they claim is comparable to a selection of [O II] emitters. We also make cuts similar to those in Favole et al. in order to compare the results for g-band-selected galaxies and [O II] emitters with their observed clustering (Section 5.2).

5.1 The correlation function and galaxy bias in real space

Fig. 13 shows the real-space two-point-correlation function, $\xi(r)$, for model galaxies at $z = 0.76$ selected following the cuts in Table 2. The different galaxy selections result in a very similar $\xi(r)$, in particular on scales above $0.1\ h^{-1}$Mpc. The same is true for the other redshifts explored. Compared to the dark matter real-space two-point-correlation function, ξ_{DM}, model galaxies follow closely the dark matter clustering for comoving separations greater than $\sim 1 h^{-1}$Mpc. The real-space bias, $\sqrt{\xi_{gg}/\xi_{DM}}$, is practically unity and constant for comoving separations greater than $2 h^{-1}$Mpc. In comparison, SDSS luminous red galaxies (LRGs) have a bias of $\sim 1.7\, \sigma_8(0)/\sigma_8(z)$.[13] From a pilot study, eBOSS ELGs are expected to be linearly biased, with a bias of $\sim 1.0\, \sigma_8(0)/\sigma_8(z)$ (Dawson et al. 2016). For the cosmology assumed in this study, eBOSS LRGs are then expected to have a bias of 2.7 at $z = 1$ and ELGS have $b = 1.62$ at the same redshift.[14]

Fig. 14 shows the evolution of the bias over the redshift range of interest for this study for DEEP2 model galaxies. For both DEEP2

---

[13] $\sigma_8(z)$ gives the normalization of the density fluctuations in linear theory and has a value of 0.81 at $z = 0$ for the cosmology assumed in this work.
[14] The ratio $\sigma_8(0)/\sigma_8(z)$ has been obtained using the ICRAR cosmological calculator http://cosmocalc.icrar.org/.
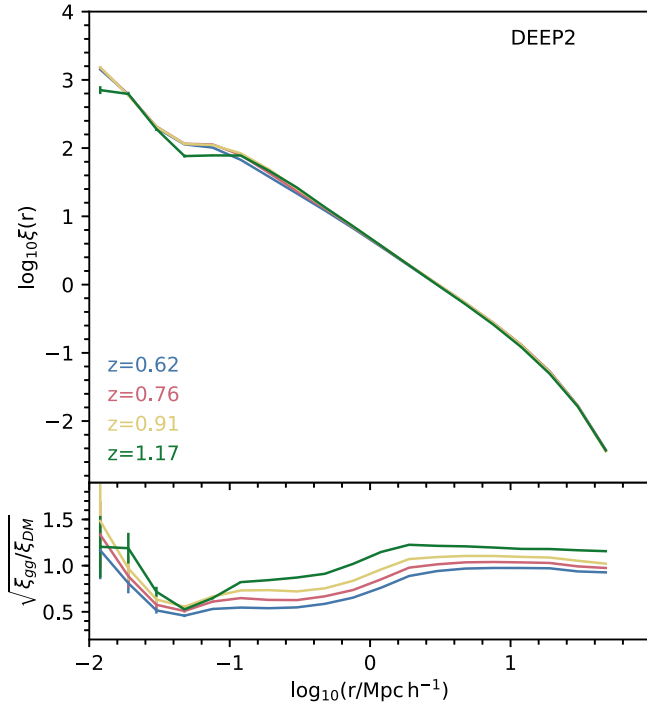
Figure 14. Top panel: the real-space two-point-correlation function for model galaxies selected with the DEEP2 cuts (see Table 2) at the redshifts indicated in the legend. Bottom panel: the real-space bias, $\sqrt{\xi_{gg}/\xi_{DM}}$, at the same redshifts. Poisson error bars are shown in both panels.
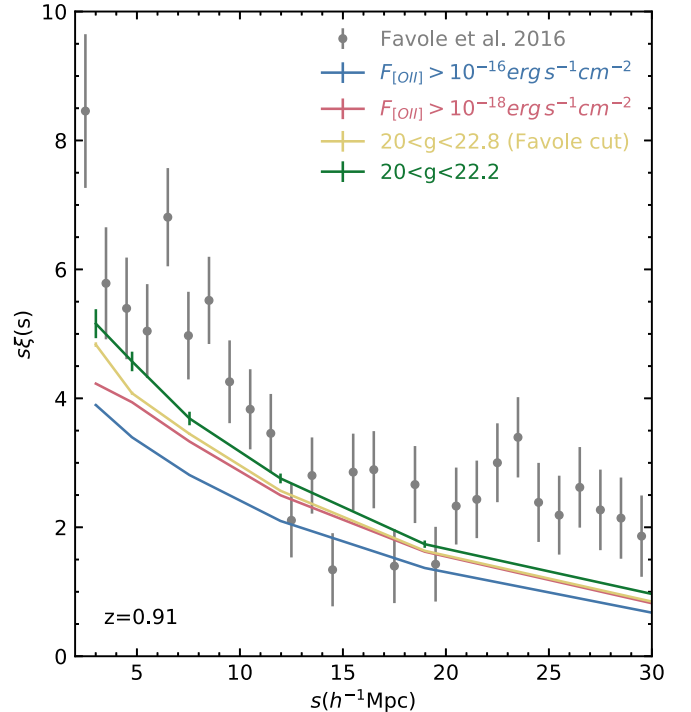

Figure 15. The predicted redshift-space two-point-correlation function, $\xi(s)$, at $z = 0.91$ plotted scaled by the comoving separation, s, as a function of s, for [O II] flux and g-band-selected galaxies as indicated in the legend. Predictions for model galaxies are shown with Poisson error bars. The grey symbols show the observational results presented in Favole et al. (2016), with error bars that include sample variance.

and VVDS-Deep selections, the bias on large scales increases by a factor of 1.2 from $z = 0.6$ to $z = 1.2$. For all the considered selections, when the propagated Poisson errors are below $\sigma_b = 0.2$, the linear bias remains between 1 and 1.4 in all cases.

Given the predicted small fraction of [O II] emitters that are satellite galaxies, these galaxies have the potential to be extraordinary cosmological probes for redshift-space distortion analysis as they are possibly almost linearly biased for the two-halo term.

5.2 The correlation function in redshift space

The redshift-space two-point-correlation function is shown in Fig. 15 for model galaxies selected with two different [O II] flux and g-band cuts. Model galaxies with a brighter [OII] flux are less clustered in both real and redshift space. This contradicts what is found observationally at $z = 0$ (Favole et al. 2016) and is related to the number of star-forming galaxy satellites in the model (see Fig. 2). Samples of model [O II] emitters are hosted by haloes with minimum masses that increase with the [O II] flux. However, the fraction of satellite [O II] emitters decreases for brighter cuts in [O II] flux. At $z = 0.91$, the percentage of satellites is reduced from 20 to 4 per cent when the selection in [O II] flux is changed from $10^{-18}\,erg\,s^{-1}\,cm^{-2}$ to $10^{-16}\,erg\,s^{-1}\,cm^{-2}$. This reduction in the numbers of model satellite galaxies in bright samples of [O II] emitters lowers the average mass of their host haloes, reducing the bias and clustering predicted by the model.

Favole et al. (2016) measured the clustering of a g-band-selected galaxy sample, with an average density of 500 galaxies per deg² in the redshift range $0.6 < z < 1.7$. The selection of galaxies based on their apparent g-band magnitude around $z = 1$ is very close to selecting ELGs. Comparat et al. (2015) showed that the g-band

magnitude is correlated to the [O II] luminosity in the studied redshift range. We also find such a correlation for [O II] emitters in the model. This correlation is due to the fact that emission lines are directly related to the rest-frame UV luminosity, as this gives a measure of the ionizing photons.

The two-point-correlation functions for galaxies with $20 < g < 22.8$ and a colour cut to remove low-redshift galaxies as measured by Favole et al. are shown with grey symbols in Fig. 15. In this figure we compare model galaxies selected with the same g-band cut to the results from Favole et al. (2016). Note that the clustering of model galaxies with $F_{[O II]} > 10^{-18}\,erg\,s^{-1}\,cm^{-2}$ and that for galaxies with $20 < g < 22.8$ overlaps for separations above $10h^{-1}$Mpc and below this separation they are comparable. The reduced χ^2 is 3.1 when comparing the clustering of model galaxies with $20 < g < 22.8$ to that of Favole et al. (2016). The reduced χ^2 decreases to ~2.6, if the g-band faint cut is changed by 0.6 mag, $20 < g < 22.2$. Model galaxies appear to be less clustered than the current observations of g-selected samples.

Favole et al. (2016) used weak lensing to estimate the typical mass of haloes hosting g-band-selected galaxies, finding $(1.25 \pm 0.45) \times 10^{12}h^{-1}$ M$_\odot$. Within the same redshift range, the model g-band sample is hosted by haloes with an average mass of ~$10^{11.8}h^{-1}$ M$_\odot$, consistent with the values reported observationally, although somewhat on the low side.

Favole et al. (2016) also estimated the fraction of satellite g-band-selected galaxies using a modified sub-halo abundance matching method that accounts for the incompleteness of small samples of galaxies that do not populate every halo. The model that best fits

their measured clustering had ~20 per cent satellite galaxies, while here we find that satellites account for only 2 per cent of our sample.

Both aspects, the lower satellite fraction and slightly lower host halo masses, contribute to explaining the lower two-point-correlation function obtained for model *g*-band-selected galaxies in comparison to the observational results from Favole et al. This result suggests that too large a fraction of model satellite galaxies are not forming stars at $z \sim 1$. In fact, even at $z = 0$ we find too large a fraction of low-mass galaxies with a very small star formation rate, compared to the observations (see Fig. 2; note that the problem is even larger for the GP14 model). The obvious place to start improving the model would be to allow satellite galaxies to retain their gas for longer, so they can have higher star formation rates on average. However, a thorough exploration of how expelled gas is reincorporated at different cosmic times might be needed (Mitchell et al. 2014; Henriques et al. 2015; Hirschmann et al. 2016).

6 CONCLUSIONS

The GP17 SA model is a new hierarchical model of galaxy formation and evolution that incorporates the merger scheme described in Simha & Cole (2017) and the gradual stripping of hot gas in merging satellite galaxies (Font et al. 2008; Lagos et al. 2014). The GP17 model also includes a simple model for emission lines in star-forming galaxies that uses the number of ionizing photons and metallicity of a galaxy to predict emission line luminosities based on the properties of a typical H II region (Stasińska 1990).

The free parameters in the GP17 model have been chosen to reproduce at $z = 0$ the rest-frame LFs in the b_J and K bands and also to improve the match to the local passive fraction of galaxies.

Using the GP17 model, we study the properties of [O II] emitters. These are the dominant ELGs selected by optical-based surveys at $0.5 < z < 1.5$. In particular, we have applied emission line flux, magnitude and colour cuts to the model galaxies to mimic five observational surveys, DEEP2, VVDS-Deep, VVDS-Wide, eBOSS and DESI, as summarized in Table 2. Over 99 per cent of the selected model [O II] emitters are actively forming stars, and over 90 per cent are central galaxies.

The GP17 LFs of model [O II] emitters are in reasonable agreement with observations (see Section 3.2). For this work, we have assumed that the dust attenuation experienced by the emission lines is the same as that for the stellar continuum. However, the assumed dust attenuation in the emission lines is expected to be a lower limit, which may alter the LF comparison.

The bright end of the LF of [O II] emitters is dominated by galaxies undergoing a starburst. The luminosity at which this population dominates depends on the interplay between the stellar and the AGN feedback.

For model galaxies, we find that the cut in [O II] luminosity removes galaxies below a certain SFR value, but that it also removes the most massive galaxies in the sample due to dust attenuation of the [O II] line (see Section 3.3).

Model [O II] emitters are typically hosted by haloes with masses above $10^{10.3} h^{-1} \mathrm{M}_\odot$ and mean masses in the range $10^{11.41} \leq M_{\mathrm{halo}} (h^{-1} \mathrm{M}_\odot) \leq 10^{11.78}$ (see Table 3). For haloes with $M_{\mathrm{halo}} \sim 10^{12.5} \mathrm{M}_\odot h^{-1}$, model [O II] emitters have median stellar masses a factor of 1.5 above the global population. This is driven by the cut on [O II] luminosity being directly translated into a cut in SFR, which in turn is correlated with stellar mass, and thus low-mass galaxies are also being removed from the selection.

As expected for star-forming galaxies, the mean halo occupation of central [O II] emitters, $\langle N \rangle_{\mathrm{[O\,II]\,cen}}$, cannot be described by a step function that reaches unity above a certain host halo mass (the typical shape for mass-selected galaxies). The $\langle N \rangle_{\mathrm{[O\,II]\,cen}}$ can be approximately decomposed into an asymmetric Gaussian for central disc galaxies, i.e. with bulge-to-mass ratio below 0.5, and a smoothly rising step function for central spheroids, which, in general, would not reach unity (see Section 4.3). This last point implies that not every dark matter halo is expected to host an ELG and it is particularly relevant for HOD models used to populate very large dark matter simulations with cosmological purposes.

Model [O II] emitters at $z \sim 1$ have a real-space two-point-correlation function that closely follows that of the underlying dark matter above separations of $1 h^{-1}$ Mpc, resulting in a linear bias close to unity. This is lower than the preliminary results for eBOSS ELGs by a factor of ~1.6 (see Section 5.1).

We have compared the clustering of *g*-band-selected model galaxies with the observational results from Favole et al. (2016), who argue that the cut $20 < g < 22.8$ selects ELGs at $0.6 < z < 1$, once an additional colour cut is applied to remove lower redshift galaxies. The typical mass of haloes hosting such *g*-band-selected galaxies as inferred from weak lensing in Favole et al. is consistent with the values we find for our corresponding model galaxies (see Section 5.2). However, our model *g*-band-selected galaxies are slightly less clustered in redshift space compared to the findings of Favole et al. (2016). This is mostly due to the smaller fraction of *g*-band-selected satellites in GP17, ~2 per cent, compared to their ~20 per cent. Favole et al. inferred the satellite fraction from a modified sub-halo abundance matching model that accounts for incompleteness, as not all haloes above a certain mass contain a *g*-band-selected galaxy. This is an indication that too large a fraction of model satellite galaxies are not forming stars at $z \sim 1$. This suggests that our model of galaxy formation and evolution can be improved by allowing satellite galaxies to retain their hot halo gas for longer, so their average star formation range is increased. However, other possibilities should be also explored, such as the reincorporation of expelled gas through cosmic time, which will most likely also have an impact on the selection of star-forming satellite galaxies.

Future theoretical studies of ELGs will benefit from the use of a more realistic model for the mechanisms that produce ELGs. Given the small fraction of [O II] emitters that are satellite galaxies, ELGs have the potential to become ideal candidates for redshift-space distortion studies at different cosmic times due to the ease of modelling their clustering. However, the non-canonical shape of their mean halo occupation distribution should be studied and may be accounted for in cosmological studies.

REFERENCES

Alonso D., 2012, preprint (arXiv 1210.1833)

Anders P., Fritze-v. Alvensleben U., 2003, A&A, 401, 1063

Baldry I. K. et al., 2012, MNRAS, 421, 621

Bauer A. E. et al., 2013, MNRAS, 434, 209

Baugh C. M., 2006, Rep. Progress Phys., 69, 3101

Baugh C. M., Lacey C. G., Frenk C. S., Granato G. L., Silva L., Bressan A., Benson A. J., Cole S., 2005, MNRAS, 356, 1191

Behroozi P. S., Conroy C., Wechsler R. H., 2010, ApJ, 717, 379

Belfiore F. et al., 2017, MNRAS, 466, 2570

Benson A. J., 2010, Phys. Rep., 495, 33

Berlind A. A. et al., 2003, ApJ, 593, 1

Bower R. G., Benson A. J., Malbon R., Helly J. C., Frenk C. S., Baugh C. M., Cole S., Lacey C. G., 2006, MNRAS, 370, 645

Bruzual A. G., Charlot S., 1993, ApJ, 405, 538

Bruzual G., Charlot S., 2003, MNRAS, 344, 1000

Calzetti D., 1997, AJ, 113, 162

Campbell D. J. R. et al., 2015, MNRAS, 452, 852

Chabrier G., 2003, PASP, 115, 763

Ciardullo R. et al., 2013, ApJ, 769, 83

Cole S., Aragon-Salamanca A., Frenk C. S., Navarro J. F., Zepf S. E., 1994, MNRAS, 271, 781

Cole S., Lacey C. G., Baugh C. M., Frenk C. S., 2000, MNRAS, 319, 168

Comparat J. et al., 2013, MNRAS, 433, 1146

Comparat J. et al., 2015, A&A, 575, A40

Comparat J. et al., 2016a, A&A, 592, A121

Comparat J. et al., 2016b, MNRAS, 461, 1076

Conroy C., Wechsler R. H., Kravtsov A. V., 2006, ApJ, 647, 201

Conroy C., Gunn J. E., White M., 2009, ApJ, 699, 486

Contreras S., Baugh C. M., Norberg P., Padilla N., 2013, MNRAS, 432, 2717

Contreras S., Baugh C. M., Norberg P., Padilla N., 2015, MNRAS, 452, 1861

Cowley W. I., Lacey C. G., Baugh C. M., Cole S., 2016, MNRAS, 461, 1621

Dalton G. et al., 2014, Proc. SPIE, 9147, 91470L

Dawson K. S. et al., 2016, AJ, 151, 44

De Barros S., Reddy N., Shivaei I., 2016, ApJ, 820, 96

de Jong R. S. et al., 2014, Proc. SPIE, 9147, 91470M

Delubac T. et al., 2017, MNRAS, 465, 1831

DESI Collaboration et al., 2016a, preprint (arXiv:1611.00036)

DESI Collaboration et al., 2016b, preprint (arXiv1611.00037)

Dickey C. M. et al., 2016, ApJ, 828, L11

Drake A. B. et al., 2013, MNRAS, 433, 796

Driver S. P. et al., 2012, MNRAS, 427, 3244

Fanidakis N., Baugh C. M., Benson A. J., Bower R. G., Cole S., Done C., Frenk C. S., 2011, MNRAS, 410, 53

Favole G. et al., 2016, MNRAS, 461, 3421

Fioc M., Rocca-Volmerange B., 1999, preprint (astro-ph/9912179)

Font A. S. et al., 2008, MNRAS, 389, 1619

Franx M., van Dokkum P. G., Förster Schreiber N. M., Wuyts S., Labbé I., Toft S., 2008, ApJ, 688, 770

Furlong M. et al., 2015, MNRAS, 450, 4486

Geach J. E., Sobral D., Hickox R. C., Wake D. A., Smail I., Best P. N., Baugh C. M., Stott J. P., 2012, MNRAS, 426, 679

Gilbank D. G., Baldry I. K., Balogh M. L., Glazebrook K., Bower R. G., 2010, MNRAS, 405, 2594

González J. E., Lacey C. G., Baugh C. M., Frenk C. S., Benson A. J., 2009, MNRAS, 397, 1254

Gonzalez-Perez V., Lacey C. G., Baugh C. M., Frenk C. S., Wilkins S. M., 2013, MNRAS, 429, 1609

Gonzalez-Perez V., Lacey C. G., Baugh C. M., Lagos C. D. P., Helly J., Campbell D. J. R., Mitchell P. D., 2014, MNRAS, 439, 264 (GP14)

Granato G. L., Lacey C. G., Silva L., Bressan A., Baugh C. M., Cole S., Frenk C. S., 2000, ApJ, 542, 710

Guo Q., White S., Angulo R. E., Henriques B., Lemson G., Boylan-Kolchin M., Thomas P., Short C., 2013, MNRAS, 428, 1351

Guo Q. et al., 2016, MNRAS, 461, 3457

Henriques B. M. B., White S. D. M., Thomas P. A., Angulo R., Guo Q., Lemson G., Springel V., Overzier R., 2015, MNRAS, 451, 2663

Hirschmann M., De Lucia G., Fontanot F., 2016, MNRAS, 461, 1760

Izotov Y. I., Thuan T. X., 1998, ApJ, 500, 188

Izotov Y. I., Thuan T. X., Lipovetsky V. A., 1994, ApJ, 435, 647

Izotov Y. I., Thuan T. X., Lipovetsky V. A., 1997, ApJS, 108, 1

Jiang L., Helly J. C., Cole S., Frenk C. S., 2014, MNRAS, 440, 2115

Kaasinen M., Bian F., Groves B., Kewley L., Gupta A., 2016, MNRAS, 465, 3220

Kauffmann G., White S. D. M., Guiderdoni B., 1993, MNRAS, 264, 201

Kennicutt R. C., Jr, 1983, ApJ, 272, 54

Kewley L. J., Geller M. J., Jansen R. A., 2004, AJ, 127, 2002

Khostovan A. A., Sobral D., Mobasher B., Best P. N., Smail I., Stott J. P., Hemmati S., Nayyeri H., 2015, MNRAS, 452, 3948

Khostovan A. A. et al., 2017, MNRAS, preprint (arXiv1705.01101)

Komatsu E. et al., 2011, ApJS, 192, 18

Lacey C., Cole S., 1993, MNRAS, 262, 627

Lacey C., Silk J., 1991, ApJ, 381, 14

Lacey C. G. et al., 2016, MNRAS, 462, 3854

Lagos C. D. P., Lacey C. G., Baugh C. M., Bower R. G., Benson A. J., 2011, MNRAS, 416, 1566

Lagos C. D. P., Baugh C. M., Zwaan M. A., Lacey C. G., Gonzalez-Perez V., Power C., Swinbank A. M., van Kampen E., 2014, MNRAS, 440, 920

Laureijs R. et al., 2011, preprint (arXiv:1110.3193)

Le Fèvre O. et al., 2013, A&A, 559, A14

Leauthaud A. et al., 2007, ApJS, 172, 219

Levi M. et al., 2013, preprint (arXiv:1308.0847)

Lilly S. J., Le Fevre O., Hammer F., Crampton D., 1996, ApJ, 460, L1

Ly C. et al., 2007, ApJ, 657, 738

McCarthy I. G., Frenk C. S., Font A. S., Lacey C. G., Bower R. G., Mitchell N. L., Balogh M. L., Theuns T., 2008, MNRAS, 383, 593

McCullagh N., Norberg P., Cole S., Gonzalez-Perez V., Baugh C., Helly J., 2017, MNRAS, in press (arXiv1705.01988)

Madau P., Ferguson H. C., Dickinson M. E., Giavalisco M., Steidel C. C., Fruchter A., 1996, MNRAS, 283, 1388

Merson A. I., Baugh C. M., Gonzalez-Perez V., Abdalla F. B., Lagos C. d. P., Mei S., 2016, MNRAS, 456, 1681

Mitchell P. D., Lacey C. G., Cole S., Baugh C. M., 2014, MNRAS, 444, 2637

Mitchell P. D., Lacey C. G., Baugh C. M., Cole S., 2016, MNRAS, 456, 1459

Mostek N., Coil A. L., Moustakas J., Salim S., Weiner B. J., 2012, ApJ, 746, 124

Mostek N., Coil A. L., Cooper M., Davis M., Newman J. A., Weiner B. J., 2013, ApJ, 767, 89

Moster B. P., Naab T., White S. D. M., 2013, MNRAS, 428, 3121

Moustakas J., Kennicutt Jr R. C., Tremonti C. A., 2006, ApJ, 642, 775

Newman J. A. et al., 2013, ApJS, 208, 5

Norberg P. et al., 2002, MNRAS, 336, 907

Okada H. et al., 2016, PASJ, 68, 47

Orsi A., Lacey C. G., Baugh C. M., Infante L., 2008, MNRAS, 391, 1589

Orsi A., Baugh C. M., Lacey C. G., Cimatti A., Wang Y., Zamorani G., 2010, MNRAS, 405, 1006

Orsi Á., Padilla N., Groves B., Cora S., Tecce T., Gargiulo I., Ruiz A., 2014, MNRAS, 443, 799

Osterbrock D. E., Ferland G. J., 2006, Astrophysics of Gaseous Nebulae and Active Galactic Nuclei. University Science Books, Mill Valley, CA

Pozzetti L. et al., 2016, A&A, 590, A3

Raichoor A. et al., 2017, MNRAS, 471, 3955

Rodríguez-Puebla A., Primack J. R., Avila-Reese V., Faber S. M., 2017, MNRAS, 470, 651

Sanchez S. F. et al., 2015, A&A, 574, A47

Simha V., Cole S., 2017, MNRAS, 472, 1392

Sobral D., Best P. N., Matsuda Y., Smail I., Geach J. E., Cirasuolo M., 2012, MNRAS, 420, 1926

Sobral D., Stroe A., Koyama Y., Darvish B., Calhau J., Afonso A., Kodama T., Nakata F., 2016, MNRAS, 458, 3443

Somerville R. S., Davé R., 2015, ARA&A, 53, 51

Somerville R. S., Primack J. R., 1999, MNRAS, 310, 1087

Stasińska G., 1990, A&AS, 83, 501

Takada M. et al., 2014, PASJ, 66, R1

Vale A., Ostriker J. P., 2004, MNRAS, 353, 189

Weinmann S. M., Kauffmann G., van den Bosch F. C., Pasquali A., McIntosh D. H., Mo H., Yang X., Guo Y., 2009, MNRAS, 394, 1213

White S. D. M., Frenk C. S., 1991, ApJ, 379, 52

Zhao G.-B. et al., 2016, MNRAS, 457, 2377

Zheng Z. et al., 2005, ApJ, 633, 791

APPENDIX A: COLOUR CUTS

Fig. A1 presents the location of model galaxies at redshifts $z = 0.62$, 0.76, 0.91, 1.17, 1.5 in the $(g - r)_{\mathrm{DECam}}$ versus $(r - z)_{\mathrm{DECam}}$, colour–colour space, compared to the regions delimited by the colour cuts *decam180* described in Comparat et al. (2016a) and summarized in Table 2 as eBOSS, top panel, and the DESI selection (DESI Collaboration et al. 2016a), bottom panel. The top panel shows model galaxies with $\mathrm{Flux_{[OII]}} > 10^{-16} \mathrm{erg\,s^{-1}\,cm^{-2}}$ and $22.1 < g_{AB}^{\mathrm{DECam}} < 22.8$. This magnitude cut mostly removes red galaxies from the colour–colour plot in Fig. A1. The bottom panel shows model galaxies with $\mathrm{Flux_{[OII]}} > 8 \times 10^{-17} \mathrm{erg\,s^{-1}\,cm^{-2}}$ and $r_{AB}^{\mathrm{DECam}} < 23.4$. The colours of model galaxies are roughly consistent with the regions defined tentatively for eBOSS (Comparat et al. 2016a) and DESI (DESI Collaboration et al. 2016a) to select ELGs at $z \sim 1$. A more detailed comparison shows the model $(g - r)_{\mathrm{DECAM}}$ to be just about 0.2 mag redder than the observations presented in Comparat et al. (2016a).

In the selection of model galaxies we use total magnitudes. The difference with respect to SDSS model magnitudes is expected to be less than 10 per cent for most model galaxies (González et al. 2009).

Fig. A1 also shows the location of stars in the $(g - r)_{\mathrm{DECam}}$ versus $(r - z)_{\mathrm{DECam}}$ space (data from Leauthaud et al. 2007, cross-matched with the COSMOS DR3 legacy survey). These overlap with the region occupied by galaxies at $z = 0.62$ and for the bluest galaxies at $0.6 < z < 1.6$. Both the eBOSS and DESI selections reported here are trading off selecting high-redshift galaxies while minimizing the stellar contamination.
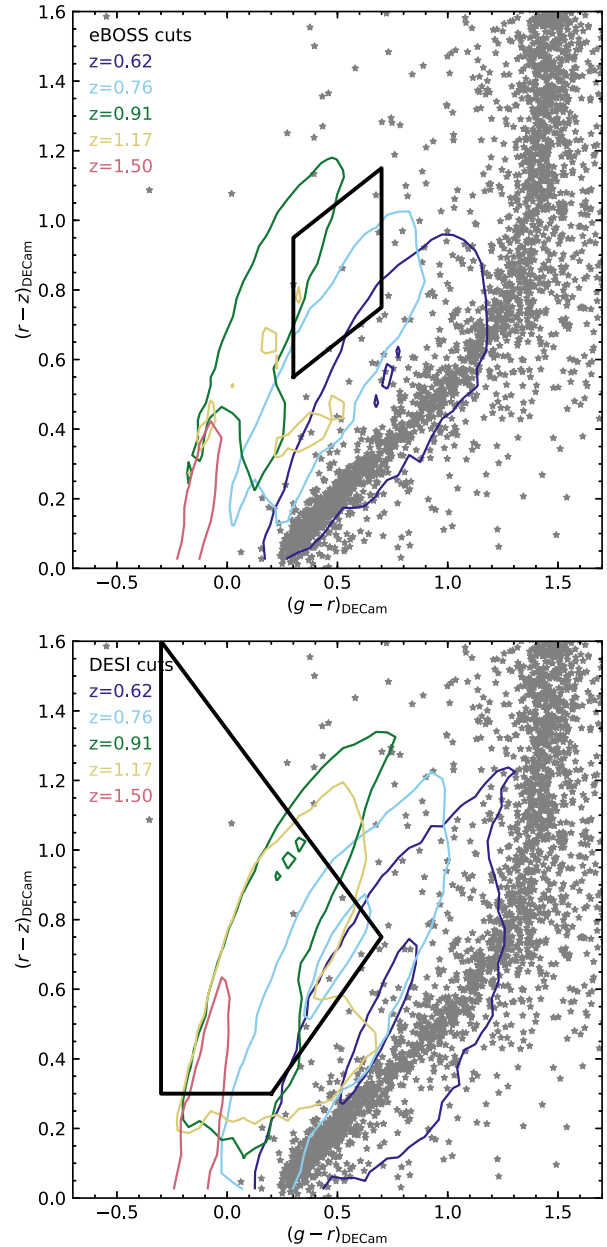

Figure A1. DECam $(g - r)$ versus $(r - z)$ parameter space with the isodensity lines at $\log_{10}(\Phi/\mathrm{Mpc^{-3}}h^3\mathrm{dlog_{10}L}) = -4.5, -1.5$ for model galaxies, with $\mathrm{Flux_{[OII]}} > 10^{-16} \mathrm{erg\,s^{-1}\,cm^{-2}}$ and $22.1 < g_{AB}^{\mathrm{DECam}} < 22.8$ (top panel) and $\mathrm{Flux_{[OII]}} > 8 \times 10^{-17} \mathrm{erg\,s^{-1}\,cm^{-2}}$ and $r_{AB}^{\mathrm{DECam}} < 23.4$ (bottom panel) at the redshifts indicated in the legend. The polygons indicate the region enclosed by the eBOSS (top panel) and DESI colour cuts (bottom panel) as summarized in Table 2. The grey symbols in both panels show the location of stars.

This paper has been typeset from a TₑX/LATₑX file prepared by the author.